ORIGINAL ARTICLE

Journal Section

Capturing experimental properties in computationally efficient faceted titania nanoparticle models

Gil M. Repa[1] | **Lisa A. Fredin**[1]

[1]Department of Chemistry, Lehigh University, PA 18015, USA

Correspondence
Lisa A. Fredin, Department of Chemistry, Lehigh University, PA 18015, USA
Email: lafredin@lehigh.edu

Funding information
Lehigh University and research computing resources provided by Lehigh University and the TG-CHE190011 allocation from Extreme Science and Engineering Discovery Environment (XSEDE), which is supported by National Science Foundation grant number ACI-1548562 and the NSF CC* Compute program through grant OAC-2019035.

Understanding the surface chemistry of nanostructured TiO_2 has long been a priority to improve photochemical device efficiency. Faceted nanoparticles, characterized by known facets not at thermodynamically ideal ratios, are particularly challenging to model due to the large number of chemical and computational parameters that must be chosen for which there is no experimental guidance. This research supplies a modeling framework for faceted TiO_2 nanoparticles that provides rationale for such decisions. By performing full DFT optimization and characterization on a series of inter-related anatase TiO_2 nanoparticles displaying {101}, (001), and {010} facets with sizes up to 202 TiO_2 units, parameter space is mapped with regard to particle size, shape, defects, and optimization protocol. Specifically, it is shown that pre-optimization is necessary in order to achieve a sufficiently delocalized electronic structure, and the increased reorganization afforded by removing higher coordinated Ti atoms compensates the high formation energy of creating these defects. Furthermore, by characterizing differently shaped nanoparticles with the same number of TiO_2 units, this research provides direct observation of shape effects on nanoparticles.

KEYWORDS

nanoparticles, TiO_2, DFT, facets, amorphous, pre-optimization, vacancies

1 | INTRODUCTION

Nanostructured TiO_2 has received intense investigation as a catalyst or support in a wide variety of photochemical applications, including dye-sensitized solar cells [1;2], water-splitting [3;4] and CO_2 reduction [5;6]. Considering this technological interest, extensive scientific effort has been spent studying the surface properties of nanostructured TiO_2 in order to achieve a fundamental understanding of the mechanisms that drive device function, as well as provide a means to tailor properties as a function of morphology. Consequently, a wide range of structurally diverse TiO_2 nanostructures with vastly varying photophysical properties have been reported [7;8;9;10;11]. Such advancement in targeted synthesis of nanoparticles with desirable properties can greatly improve device efficiency, yet a unifying model that relates nanoparticle structural features to specific electronic properties *a priori* to speed design to implementation time continues to elude researchers.

In pursuit of such ambitions, experimental study is inherently limited by the fact that observations are ensemble averages over a wide range of structural features. Thus, the problem of untangling structure-function relationships is well-suited for computational study, where quantum mechanics can predict the properties of contrived nanoparticles varying along a single structural axis, such as exposed facets or size. However, even considering recent advancements in computational infrastructure, full quantum mechanical calculations of experimentally-sized nanoparticles in the 10-100 nm range [12] is beyond what is practical with DFT. Thus, developing chemically accurate models that simultaneously capture the properties of experimentally-sized particles while residing in a computationally tractable size regime is non-trivial.

The problem is further confounded by difficulties capturing the diverse range of structural features that have been observed in real nanoparticles in such model systems. Indeed, previous successes in computational modelling of TiO_2 nanoparticles have largely focused on idealized periodic surfaces [5;13], spherical radially symmetric particles [14;15], or Wulff-shaped particles [16], which in the case of the anatase of TiO_2 is an octahedron composed of eight {101} facets. While such studies have done much to advance nanostructured TiO_2 technologies, the same understanding has yet to be extended to more complex nanostructures. In particular, particles that are characterized by known low index facets, yet not at thermodynamically ideal shapes or ratios, and hereby referred to generally as faceted nanoparticles.

Previous research to probe the structure-property relationship of faceted TiO_2 nanoparticles has largely been focused on modifications to ideal Wulff-shaped particles, either truncating or elongating the octahedra to introduce additional (001) or {010} facets respectively [17;18;19;20;21]. Many studies have utilized small faceted nanoparticles intended to represent larger surfaces for adsorption studies [22;23]. With regard to larger clusters, Lundqvuist et al. [24] documented the electronic properties and adsorption characteristics of variously shaped anatase nanoclusters with up to 68 TiO_2 units. Using LDA, Wang and Lewis [25] were able to study the effect of particle size and dimensions on a series of faceted particles composed of {101} and (001) facets up to 774 atoms. However, due to the computational effort required for these studies, the number of cluster shapes that can be studied are limited, and thus it is difficult to know the extent for which a particular particle model be accurately applied. To gain a better understanding of the effect of particle morpholgy on calculated properties, Gałyńska and Persson [26] successfully mapped the electronic properties of a set of 34 $(TiO_2)_n$ clusters, with sizes of anatase nanoparticles up to 122 TiO_2 units. Most of these studies draw conclusions by comparing particles with different numbers of TiO_2 units, introducing a confounding variable when attempting to attach particular properties to specific molecular geometries.

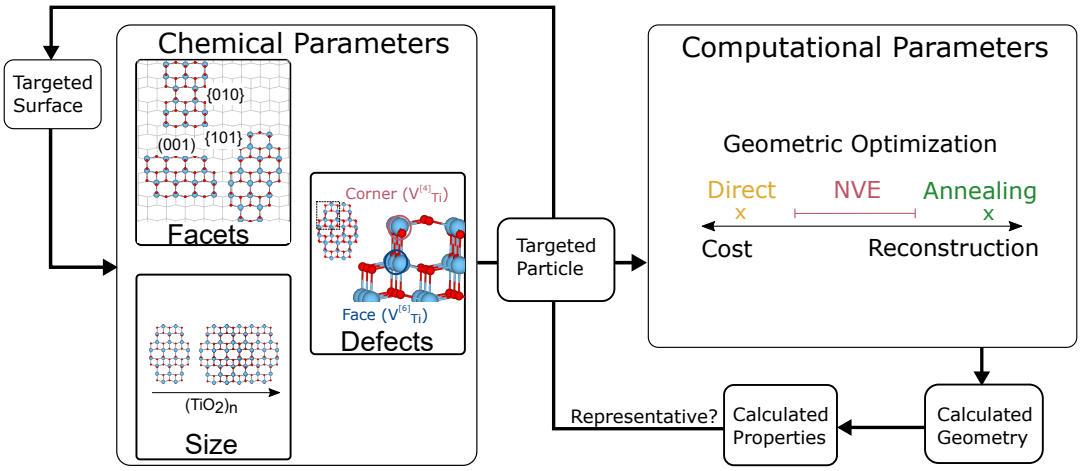

FIGURE 1 Interplay between chemical and computational choices in building faceted nanoparticle models.

In this work, we extensively explored chemical and computational parameters by mapping the electronic and geometric properties of several different nanoshapes with identical molecular formulas ranging from 60 to 202 TiO_2 units and quantifying how different model preparations can affect calculated results to produce models that produce experimentally relevant properties. We show that perturbation of the nanoparticle crystal away from the cut crystal structure through pre-optimization with classical molecular dynamics simulations (MD) and vacancies of higher-coordinated Ti atoms can simultaneously lower computational effort, as well as produce a more delocalized electronic structure, which is critical to represent the band structures of larger experimental nanoparticles.

1.1 | Modeling Faceted Particles

Developing models of faceted nanoparticles, which are characterized by well-defined surfaces not at thermodynamically ideal ratios or shapes, is significantly more complex than for Wulff- or spherically-shaped particles. This is a multi-pronged challenge, because not only is there a much greater range of chemically valid nanoshapes that must be considered, there are also numerous modeling choices that must be made for which there is no experimental guidance. Such decisions may lead to vastly different calculated results. Therefore, careful model development like that presented here is critical to ultimately provide rationale for how to build models for future studies of faceted nanoparticles. In this section, we review the choices that must be made along with the inter-dependence of each of these choices (Fig. 1).

In general, faceted nanoparticles are created through a top-down approach, which involves carving a particular nanoparticle from bulk anatase. Particle shape is largely driven by desire to study a specific facet. The three most experimentally relevant facets for anatase TiO_2 are the (001), {101}, {010} facets, although higher index surfaces are possible[27]. When creating nanoparticles targeting a particular facet, arbitrary choices regarding the nature of the facet intersections and ratios between facets is inevitable, and thus must be accounted for when considering results between varying particles. The number of atoms feasible for quantum mechanical calculation restrict particle sizes to only a few nm at best, which represent only the smallest nanoparticles measured in experiment. Thus, model development is further tasked with developing models that are simultaneously small enough to be amenable to DFT calculation, while being representative of larger systems.

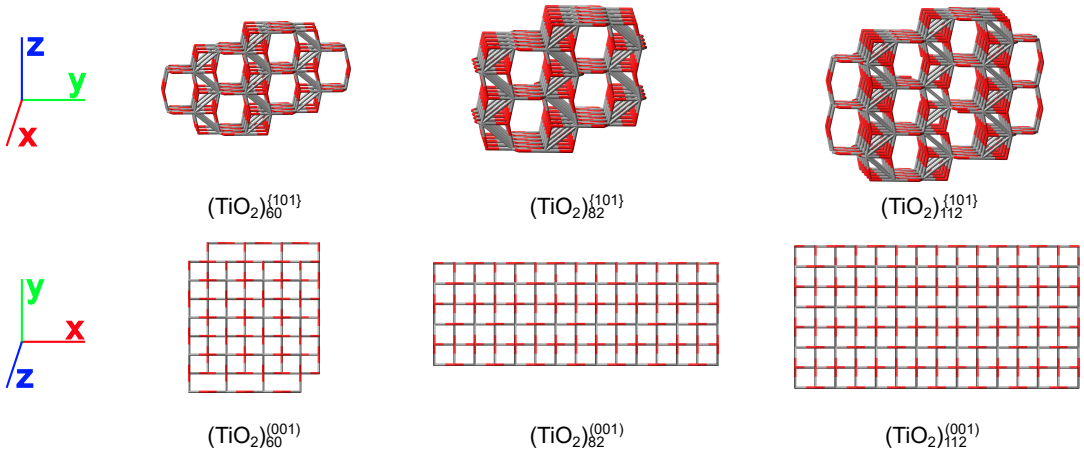

FIGURE 2 Unoptimized $(TiO_2)_n^{\{101\}}$ (top panel) and $(TiO_2)_n^{(001)}$ (bottom panel) nanoparticles.

The relationship between number of atoms comprising a nanoparticle, and emergence of size-dependent properties is not straightforward. Specifically, the shape of equivalently sized nanoparticles can be a major determinant of nanoparticle properties. Real nanoparticles are characterized by both bulk-like crystalline cores and localized surface states. Therefore, budgeting the number of atoms to achieve both core and surface regions is critical for experimentally accurate nanoparticle models. In addition to considering the surface area to volume ratio, consideration must be made for the size of a particle in an individual dimension, and whether asymmetric particles elongated in a single dimension, such as nanorods, are computationally preferable to more symmetric ones. In addition, faceted nanoparticles can be of any point group, whereas Wulff particles are d_{2h} and spherical particles are radially symmetric in all dimensions.

The type and amount of exposed facets produced by carving from the bulk will have a direct impact of stoichiometry of the resultant nanoparticle. In general, all nanoparticles other than the ideal octahedral Wulff particle will require removal of Ti atoms in order to achieve Ti/O stoichiometry. Consequently, the choice of which Ti atoms to remove, and how to handle the resultant dangling singly coordinated O ($^{[1]}$O) must be considered. Common practice in literature until this point[17;28;29] has been to remove the least coordinated Ti atoms in accordance with thermodynamic intuition. We find that this approach may not be desirable for all cases. In particular, the least-coordinated atoms are often at the corners or edges of the nanoparticle. In real systems, these may be the most reactive sites[25], and therefore realistic models of TiO_2 catalysis require accurate descriptions of such sites. Furthermore, removal of Ti atoms from the corner sites tends to result in a higher number of $^{[1]}$O and their close proximity to each other at the corner of the nanoparticle may create numerical issues in early self-consistent field (SCF) interations. Alternatively 5- or 6-coordinated Ti atoms from surface sites could be removed. However, while oxygen vacancies in both bulk[30] and nano-TiO_2[31] have been extensively studied, there is little information on Ti vacancies due to their generally high formation energy in bulk systems[32]. All of these modeling criteria can be regarded as "chemical choices" of the system, *i.e.*, generation of a molecular geometry possessing desired structural characteristics. Once the chemistry of interest has been determined, the remaining decisions are computational, mainly selecting the appropriate optimization strategy to obtain a low energy structure representative of the surface geometry and electronic structure of larger experimental particles.

Geometric optimization of molecular nanostructures represents one of the biggest challenges to the computa-

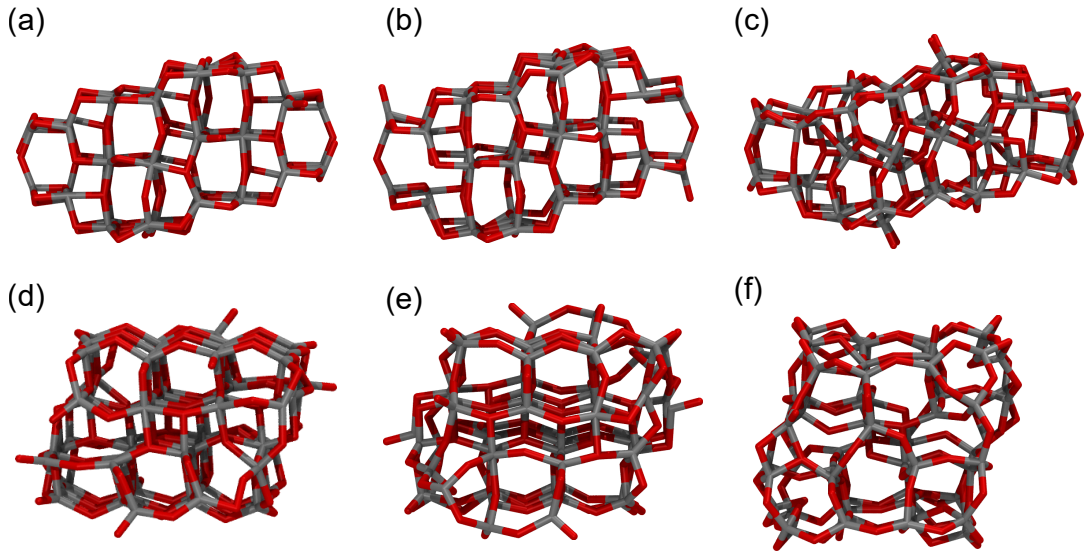

FIGURE 3 $(TiO_2)_{60}^{101}$ and $(TiO_2)_{60}^{001}$ prepared by direct (a and d), $(NVE)_c$ (b and e), and $(NVE)_f$ optimizations (c and f).

tional community at present. The potential energy surfaces for such structures are very flat and the large number of atoms makes extensive quantum calculation spanning all possible configurations to find a global minimum impossible. Numerous techniques have been applied to tackle this issue, such as optimization using genetic algorithms or Monte Carlo simulations[33], however such approaches have not proven effective for larger clusters, and rarely result in a crystalline enough structure to be considered a faceted nanoparticle. To remove barriers to energy-lowering structural reconstructions in larger particles simulated annealing has been performed, where the nanoparticle is heated and cooled using dynamics methods. Such methods utilizing MD or tight-binding DFT methods have been ubiquitous in studying spherical nanoparticles[17;34]. However, the advantages afforded by such an approach are limited for faceted nanoparticles in the size range tractable for electronic structure calculations. In particular, this size regime with faceted surfaces likely represents a meta-stable state. Therefore, as annealing methods would likely produce amorphous TiO_2 at this size, less perturbative methods, like pre-optimization using simple inter-atomic potentials[35], for nanoparticle optimization are needed. However, the complicated choice of optimization method can drastically change calculated properties[36], even if structural deviation is minimal.

For each of these choices there is little experimental intuition to guide different model decisions. This work aims to develop a general guide for how to access nanoparticles with a large amount of either {101} or (001) facets that can be used to model larger experimental particles. This is done through a systematic evaluation of a set of interrelated nanoparticle models that probe systematic size, defects, and optimization strategies. Particles with different majority facets,sizes, and defects are built and optimized with DFT or MD + DFT. These chemical and computational choices lead to different geometric and electronic effects. In particular, special considerations must be made to access particles with a large amount of (001) surface. Throughout the paper, comparisons are made across identically sized (001) and {101} particles allowing the chemistry of different shaped TiO_2 nanoparticles to be directly probed for the first time.

2 | PARTICLE MODELS

2.1 | Particle Facets and Size

Faceted TiO_2 nanoparticles were generated by carving various nanoshapes from bulk anatase TiO_2 (Fig. 2). Nanostructures with large amounts of either {101} or (001) facet and reasonable stoichiometry were selected. A discussion of particles with a significant amount of {010} facets is presented in Sec. 3.2. These facets comprise much of the previous research on TiO_2 nanostructures and are the three most experimentally relevant surfaces [27]. The particles are referred to as either $(TiO_2)_n^{\{101\}}$ or $(TiO_2)_n^{(001)}$ depending on the majority facet and where n = number of TiO_2 units. For both groups, nanoshapes that maximized the amount of the targeted facet were generated, and sets that possessed a partner in the opposite group with an identical number of TiO_2 units are presented here. By selecting nanoparticles with the same number of TiO_2 units but varying shapes, it is possible to isolate facet effects from size effects, while allowing for discernment between general and facet-specific guidelines for modeling different TiO_2 surfaces. All particles were carved to at least the point group C_i, a feature that eases the DFT optimization procedure. To refer to the dimensions of the nanoparticles, the coordinate system where the z-axis is the normal of the facet displaying the largest amount of targeted surface area is adopted.

The most efficient shape maximizing the targeted surface-area to volume ratio is a slab that lacks significant dimension in the z-direction while maximizing x- and y-dimensions. However, the unique chemistry of nanostructures arises as a result of the coexistence of delocalized electrons in core bulk-like regions of the nanoparticle interior with localized states located on the nanoparticle surface, as previously discussed. Indeed, it is well-understood in periodic plane-wave DFT studies of nanoparticle surfaces that substantial representation of the subsurface region is necessary to achieve reliable results [37;38]. Similar effects can be expected for the discrete nanoparticle models studied here, *i.e.*, all three dimensions must be significantly large while simultaneously limiting the number of atoms to be computationally tractable. This is systematically tested in the current study to understand whether it is better to spend the atom budget on developing larger surface areas or core bulk regions. Thus for the {101} particles, we selected three different particles with different sizes (60, 82, and 112-TiO_2 units). Comparing the 60 and 82-unit particles represents an increase in primarily the x- and y- directions of the slab with dimensions 11 x 17 x 9 Å and 19 x 13 x 9 Å for $(TiO_2)_{60}^{\{101\}}$ and $(TiO_2)_{82}^{\{101\}}$, respectively. Comparing the 82 and 112 unit particles represents a change primarily in the z-direction with dimension of 15 x 17 x 13 Å for $(TiO_2)_{(112)}^{\{101\}}$. In the language of periodic slab studies, the smallest two of these nanoparticles are 3 layers thick, while the larger particle is 4 layers thick. For the $(TiO_2)_n^{(001)}$ particles, particle size is primarily controlled by varying the x-, and y-dimensions to produce particles with 13 x 15 x 8 Å, 9 x 26 x 8 Å and 13 x 26 x 8 Å dimensions for $(TiO_2)_{60}^{(001)}$, $(TiO_2)_{82}^{(001)}$, $(TiO_2)_{112}^{(001)}$ respectively. Unoptimized geometries of each of the carved particles studied in this section are available in Fig. 2. A more thorough discussion on the effect of number of layers for $(TiO_2)_n^{(001)}$ particles is presented in section 3.2.

2.2 | Particle Defects

In the case of the faceted nanoparticles studied here, creation of stoichiometric nanostructures involves deletion of extra Ti atoms from the anatase surface to create Ti vacancies (V_{Ti}). In general, the $(TiO_2)_n^{(001)}$ particles require deletion of more Ti-sites to achieve stoichiometry (Table S1). To test the effect of deleted Ti atom location and chemistry on the calculated properties and reconstruction, two different sites on each nanoparticle were selected: 3-coordinated Ti ($^{[3]}$Ti) atoms at the corners of the nanoparticles at the intersection of two {101} and one (001) surfaces (red dots in Figs. S1 and S2), and $^{[6]}$Ti on the {101} surface (blue dots in Figs. S1 and S2). These two locations were

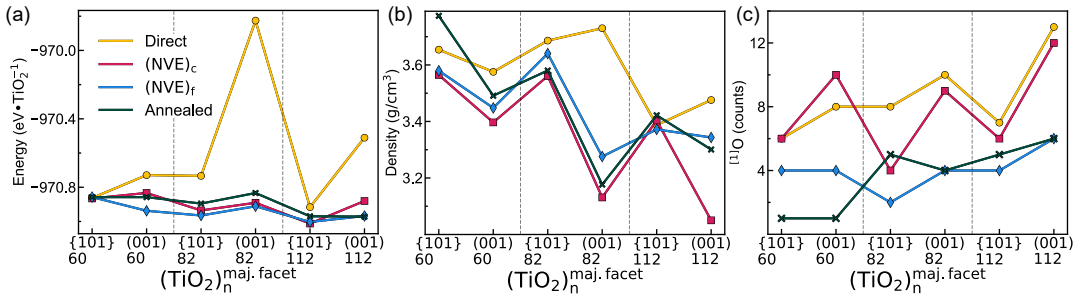

FIGURE 4 Optimization energy (a), density (b) and number of $^{[1]}$O (c) for $(TiO_2)_n^{\{101\}}$ and $(TiO_2)_n^{(001)}$ nanoparticles. The gray lines divide the data points by number of TiO_2 units. The x-axis labels reference the particle shape (maj. facet) and number of TiO_2 units, n.

chosen as they represent the least and most disruptive locations for Ti vacancies based on typical thermodynamic intuition, and an intermediate choice would've been to delete the $^{[5]}$Ti from the {101} surface. Each particle was then subjected to a brief NVE (see definition below) MD simulation followed by a DFT optimization. These particles are referred to as $(NVE)_x$ where x=c or f depending on whether the Ti atoms were removed from the corner or the face, respectively.

2.3 | Optimization

To perform a comparison of the various methods that have been used to model nanoparticles before, as well as control how much of the potential energy surface is explored, we adopted several different protocols for nanoparticle optimization. The simplest method here involves directly submitting the cut nanoparticle for DFT optimization. Such an approach explores the least amount of potential energy landscape associated with a particular guess structure, and in general, represents the most computationally expensive of the methods utilized here. In particular, these structures are highly prone to charge sloshing during early SCF cycles, and often require generating an initial guess wavefunction for the DFT optimization using Hartree-Fock. Applying a random displacement to each atom of up to 0.12 Å in any direction can lead to marginal improvement in SCF convergence during early iterations. All DFT calculations were preformed using Gaussian16 [39] with default settings. The B3LYP exchange-correlation functional [40] coupled with the effective-core potential basis set proposed by Boutelier [41], which is of double-zeta quality and provides an 18-core-electron pseudopotential for Ti atoms was used. This setup has been previously shown to produce acceptable results for faceted TiO_2 nanoparticles [24;26]. All direct optimizations were performed using particles with corner V_{Ti} described above.

To explore a larger region of the potential energy surface than that afforded by direct optimization, we tested pre-optimization with MD. A positive side effect of such approaches is that a structure closer to the energetic minimum may be used as the guess geometry for the quantum mechanical optimization, thus possibly reducing the computational cost. Such approaches using MD pre-optimizations to cheapen DFT calculations have been extensively compared and discussed before [35]. However, the primary goal of the pre-optimizations in the current work was not intended to reduce the number of DFT geometry optimization steps by matching the lowest energy structure, but rather to explore degrees of particle surface reorganization beyond that accessible to the direct optimization with DFT. The computational savings seen were primarily due to fewer SCF cycles required to reach convergence in early geometric iterations rather than less DFT optimization steps. As previously discussed, an important trade-off emerges

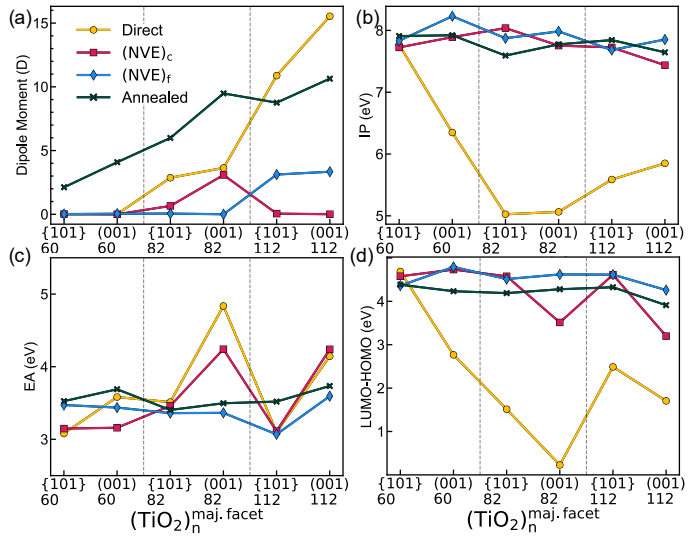

FIGURE 5 Dipole Moment (a), IP (b), EA and LUMO-HOMO (c) for $(TiO_2)_n^{\{101\}}$ and $(TiO_2)_n^{(001)}$ nanoparticles. The gray lines divide the data points by number of TiO_2 units. The x-axis labels reference the particle shape (maj. facet) and number of TiO_2 units, n.

when utilizing such methods to balance energy lowering reconstructions while retaining enough of the morphology of the cut nanoparticle such that the targeted faceted surface is well-represented.

In order to create minimal perturbation in the structure, each particle was briefly run in the micro-canoncial ensemble (NVE) that is characterized by constant energy over each microstate. This should relieve the highly strained regions of the cut nanoparticle without causing too much perturbation to the overall structure. This small pre-optimization was able to remove the numerical instabilities associated with the direct optimiziation, reducing computational cost and allowing us to access a wider number of particles that failed to optimize in DFT. These NVE runs were performed in LAMMPS[42] using the Matsui-Akaogi potential[43] for TiO_2 with a 10 Å cutoff to the coulombic contribution of the potential. Each particle geometry was first minimized in a non-periodic shrink-wrapped box until the maximum force on each atom was 1.0×10^{-3} kcal/mol-Å. This was then followed by a brief 10 ps NVE run with a 0.1 fs timestep. The resultant structure was then symmeterized to the point group of the original cut particle (C_i) using GaussView[44], and then freely optimized using the DFT method described above. However, unlike the cut particles, symmetry was applied to the initial guess and enforced during early geometry optimization cycles. In later optimization steps, particles were permitted to break symmetry.

The most aggressive approach to nanoparticle preparation that should allow exploration the entire nanoparticle potential energy surface is through simulated annealing. Such methods have largely been applied to generate amorphous phases from bulk crystalline solids[45;46]. To serve as a baseline for complete amorphicity, and thus the direct opposite of the ideal faceted particles, we additionally heated each of the cut nanoparticles. Annealed particles were prepared using the same MD potential and timestep as the NVE runs, and started from the NVE output. Each structure was heated from 800 K to 2000 K in a NVT ensemble over 5 ps. The system was then allowed to evolve for 100 ps at 2000 K, followed by cooling over 10 ps to 300 K. The resultant structure was then submitted for full DFT optimization as previously described. We subjected each of the nanoparticles in the (001) and {101} groups to all

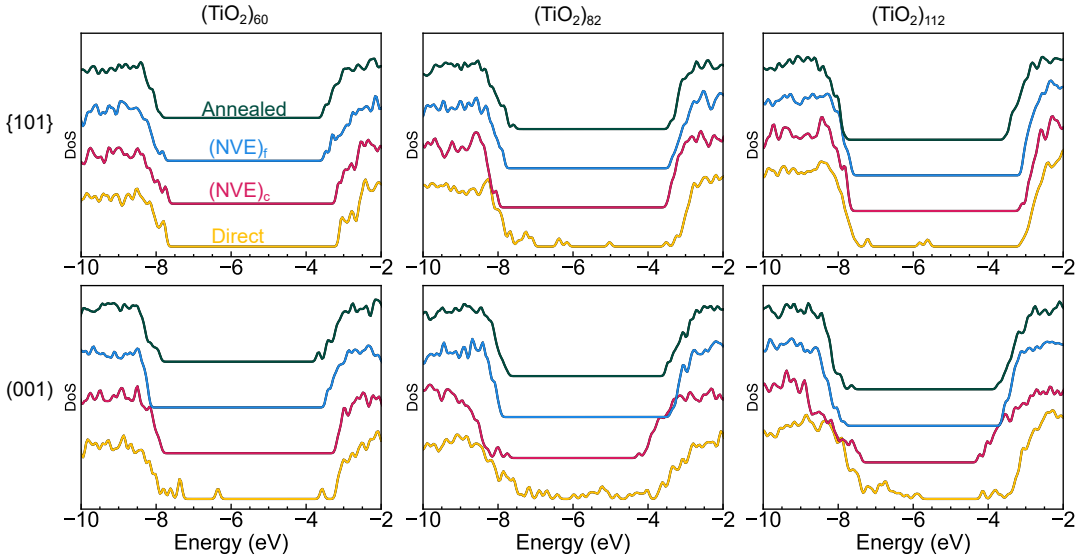

FIGURE 6 DoS for each $(TiO_2)_n^{\{101\}}$ and $(TiO_2)_n^{(001)}$ particle studied here.

of these optimization protocols to quantify the balance between ease of optimization and retaining models of the desired surface. We refer to the nanoparticles resulting from each of these preparations as either directly optimized, $(NVE)_{c/f}$, or annealed in order of increasing aggressiveness.

3 | RESULTS & DISCUSSION

3.1 | (001) vs. (101) Nanotitania Models

3.1.1 | Geometric Effects

Optimized geometries for $(TiO_2)_{60}^{\{101\}}$ and $(TiO_2)_{60}^{(001)}$ nanoparticles are available in Fig. 3 (optimized geometries for all $(TiO_2)_n^{\{101\}}$ and $(TiO_2)_n^{(001)}$ particles studied here are available in Figs. S1 and S2 respectively). Qualitatively, it is apparent that there is more disorder for each increasingly aggressive particle preparation. This fact is most exaggerated for the $(TiO_2)_n^{(001)}$ particles, likely due to the greater instability of the (001) facet[19], unstable corner and edge structures, and highly asymmetric dimensions of these particles. Indeed, many of the $(NVE)_f$ $(TiO_2)_n^{(001)}$ particles bear little resemblance to their starting geometries. Conversely, reconstruction in the $(TiO_2)_n^{\{101\}}$ is less dramatic, with reorganization of the majority of the non-annealed particles being limited to the region surrounding V_{Ti}. Even such qualitative analysis reveals that different computational considerations are necessary depending on the majority exposed facet and shape.

In general, direct optimization of the nanoparticles results in a higher energy structure opposed to those that have been treated with any MD method (energy per TiO_2 unit: Fig. 4a and Table S2). Among the directly optimized particles, there is significant energetic differences between same-sized $(TiO_2)_n^{\{101\}}$ and $(TiO_2)_n^{(001)}$ of 0.8, 91 eV, and 45 eV for 60-, 82-, and 112-unit particles respectively. The $(NVE)_c$ particles retain this trend with energetic separation between the respectively sized $(TiO_2)_n^{\{101\}}$ and $(TiO_2)_n^{(001)}$ 1.9, 3.7, and 15 eV. Both $(NVE)_f$ and annealed particles

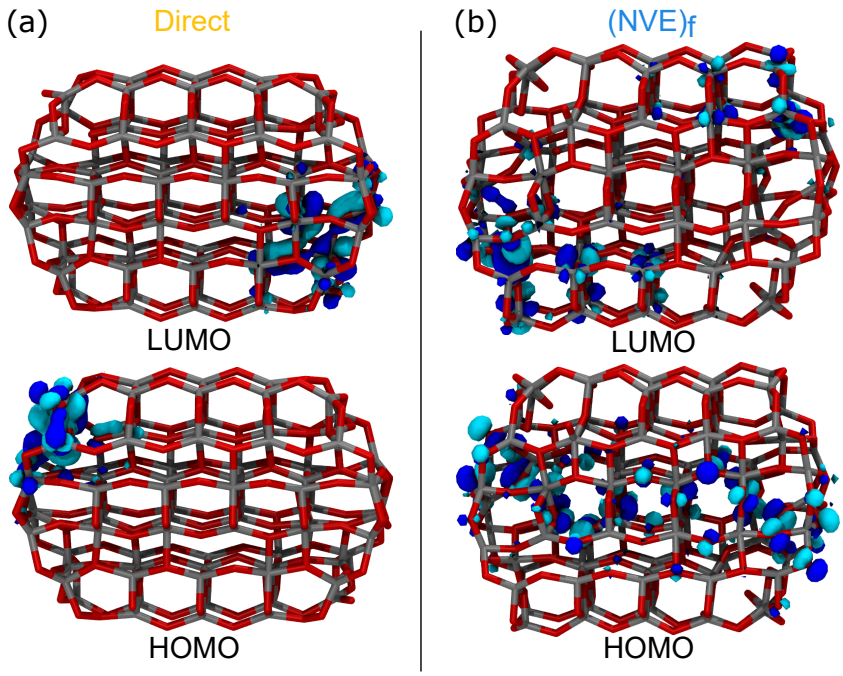

FIGURE 7 Frontier orbitals for directly optimized (a) and $(NVE)_f$ (b) $(TiO_2)_{82}^{\{101\}}$

are less sporadic in the calculated energies. This analysis, combined with lack of significant structural differences between the directly optimized and $(NVE)_c$ particles suggests that preparing particles with $(NVE)_c$ may be the ideal way to achieve models that lack the high-energy corner and edge structures while retaining largely ideal facets and no homogenization of properties.

It is notable that the most energetically favorable particles studied here are the $(NVE)_f$ particles, rather than the annealed or $(NVE)_c$ particles. Previous experimental[47] and theoretical[17] investigations have suggested approximately 2 nm as a lower limit for favorability of formation of a crystalline core in a model, which is approximately twice the size of the largest particles studied here. A possible reason for this discrepancy is the the shape of the annealed particles studied here, which possess similar dimensions of their crystalline counterparts. Most previous studies have focused on spherically cut annealed particles, which possess a much lower proportion of destabilizing surface atoms than those in the current study. A quantification of the sphericity[48] of each nanoparticle is available in Fig. S3. An additional source for this discrepancy could be related to the cooling rate utilized in the MD simulations. It is well-known that cooling rate will have a direct effect on the calculated geometry[34], however a systematic comparison of different cooling rates is beyond the scope of this work. Additional analysis of the density of each nanoparticle, calculated from Van der Waals surface of the nanoparticle (with r_{Ti}=1.76 Å and r_O=0.48 Å) confirms each of the nanoparticles studied here is far from bulk-like (Fig. 4b) with calculated densities far below the bulk anatase value of 3.90 g/cm^3. Such density lowering has been observed in amorphous particles of approximately 2 nm to have density of lowering to 3.70 g/cm^3 [47], indicating that all of these particles do not have significant core regions.

Inspection of reconstruction around the Ti vacancies of the particles reveals a number of dangling $^{[1]}$O. These regions may be critical to the electronic properties of the nanoparticle, providing favorable locations for charge localization. Furthermore, lack of reorganization in this region may lead to the increased energy of directly optimized

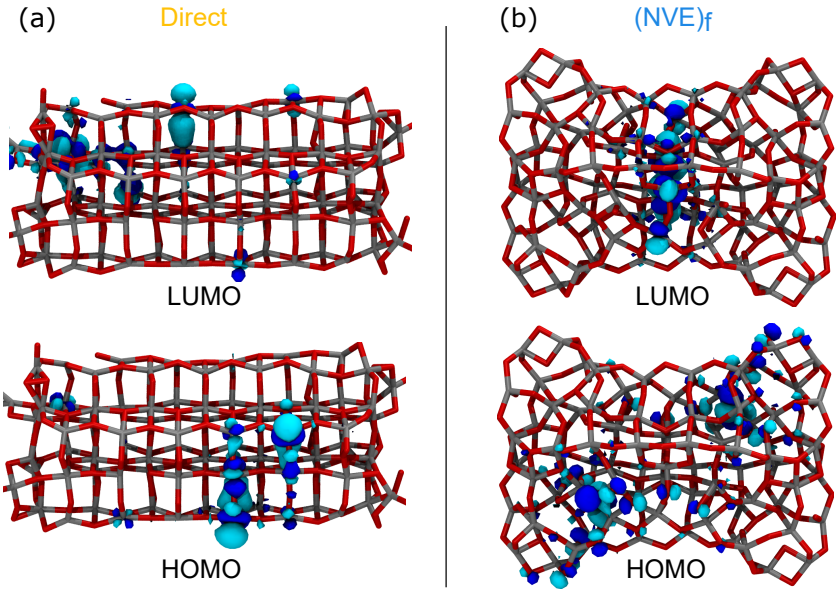

FIGURE 8 Frontier orbitals for directly optimized (a) and $(NVE)_f$ (b) $(TiO_2)_{82}^{(001)}$

particles. Therefore, the number of $^{[1]}O$ in each optimized particle is quantified (Fig. 4c). In the unoptimized structure, each corner V_{Ti} creates two $^{[1]}O$, while each face vacancy only results in one. The corner vacant particles (*i.e.*, directly optimized and $(NVE)_c$) possess a higher number of $^{[1]}O$. Differences in the structure around V_{Ti} between these two groups can be attributed to the fact that $^{[1]}O$ in the directly optimized particles simply move to occupy the Ti vacancy location, forming a very sharp approximately 46° O–Ti–O bond angle. In the $(NVE)_c$ particles, this under coordinated oxygen moves towards the neighboring Ti atom. The previous oxygen occupying this position is moved down to coordinate with the next-nearest neighbor Ti atom (Fig. S4). The appearance of the approximately 46° O–Ti–O bond angle is the only systematic difference apparent in any of the bond length or angle distributions (Figs. S5-7 and Tables S3-5). The higher values of $^{[1]}O$ in $(TiO_2)_n^{(001)}$ particles compared to $(TiO_2)_n^{\{101\}}$ particles of respective size is likely simply a result of removing more Ti atoms to maintain stoichiometry, which is an additional source of increased reorganization. Coordination statistics for Ti atoms (Fig. S8) show that the majority of species to be $^{[5]}Ti$. This indicates that surface Ti atoms are the dominant species, and even the bulkiest $(TiO_2)_{112}^{(001)}$ particle studied here is insufficient to develop a core bulk-like region geometrically. It is notable that with each increasingly aggressive preparation scheme, the average Ti atom coordination number is decreased, resulting in 5.0, 4.9, 4.8, 4.8 for direct, $(NVE)_c$, $(NVE)_f$ and annealed particles, respectively. Such trends after annealing procedures have been reported previously [17], suggesting that creation of more surface $^{[4]}Ti$ through annealing may be a viable way to increase the reactivity of a nanoparticle.

3.1.2 | Electronic Effects

Among all electronic properties, the dipole moment can potentially give insight into the subtle geometric differences between the different particle preparations. In terms of practical applications, it is directly relevant for properties such as nanoparticle aggregation [49;50], and has long been considered an indicator of the nature of a nanocrystal model [29].

Fig. 5a shows that generally both $(NVE)_{c/f}$ prepared particles do not possess a substantial dipole moment, with small exceptions occurring for the 82- and 112-unit particles. This contrasts with the annealed and directly optimized particles which both possess an increasingly large dipole moment with particle size. We attribute the higher dipole moment in the former as an effect of electron traps that may form in the amorphous material[46]. The large dipole moment in the directly optimized particles is more anomalous as structural deviation from the $(NVE)_c$ particles is minimal. Generally, this can be interpreted as an indication of the formation of localized orbitals around highly unstable surface structures. Indeed, if such is the case then the $(NVE)_c$ preparation is producing a more bulk-like particle than that of the directly optimized. Further characterization of the electronic structure is carried out in the context of Koopmans' Theorem, which allows extraction from DFT parameters that can be directly measured by experiment. Specifically, the ionization potential (IP) and electron affinity (EA) are defined as:

$$IP = -E_{HOMO}, EA = -E_{LUMO}$$

Although due to the well-known "band-gap" problem of DFT, quantitative agreement between the values calculated here and past experimental results should be interpreted with caution. The directly optimized particles predict a wide range of IPs varying over approximately 3 eV, reaching a minimum with the $(TiO_2)_{82}^{(001)}$ (Table S6). The $(NVE)_{c/f}$ and annealed particles do not show this same variation, and produce much better agreement with IP calculated in previous DFT studies[28;26]. There is similar variation among the different preparation methods in the plot of EA. However, unlike in the IP values, $(NVE)_c$ prepared particles do a better job at reproducing the trend calculated for the directly optimized particles. Specifically, there is a large difference between the directly optimized $(TiO_2)_n^{\{101\}}$ and $(TiO_2)_n^{(001)}$ particles of 0.5, 1.3, 1.0 eV for n = 60, 82, and 112 units, respectively. The $(NVE)_c$ prepared particles predict separation of 0.8 and 1.1 eV for $(TiO_2)_{82}^{\{101\}}$ with $(TiO_2)_{82}^{(001)}$ and $(TiO_2)_{112}^{\{101\}}$ with $(TiO_2)_{112}^{(001)}$, respectively (Table S7). These patterns in IP and EA naturally manifest in the LUMO-HOMO gaps, which perhaps provide the best insight into different electronic characteristics among the different preparations. This value is quite erratic for the directly optimized particles, reaching near metallicity for the $(TiO_2)_{82}^{(001)}$ particle (Table S8). Previous DFT calculations have predicted similar results for comparably shaped nanostructures, such as the nanoribbons studied by Lino et al.[51] However, this is a critical sign that direct optimization of nanoparticles in a computationally tractable size range is insufficient for preparing nanoparticle models representative of larger structures. Across the $(NVE)_c$ prepared particles, $(TiO_2)_n^{\{101\}}$ particles in general predict a smaller LUMO-HOMO gap than respectively sized $(TiO_2)_n^{(001)}$ particles. The facet-dependence of LUMO-HOMO gap is mostly removed for the $(NVE)_f$ and annealed particles, however the latter continues to predict an approximately 0.4 eV larger LUMO-HOMO gap.

For further insight into nature of the band edges, the Inverse Participation Ratio (IPR) is calculated for each orbital. This metric has been commonly employed to investigate amorphous materials in planewave DFT calculations[46], and can be regarded as a measure of the localization of a particular molecular orbital. We adapt the IPR to the suit the atom-centered basis set employed in the current study for the i^{th} molecular orbital ψ_i as:

$$IPR(\psi_i) = \frac{\phi_j^4}{(\psi_i^2)^2}$$

Where ϕ_j is the sum of absolute values of the basis set coefficients contributed by the j^{th} atom and ψ_i is calculated by the sum of the absolulte values of all the basis set coefficents of the particle molecular orbital. Therefore, a higher value in the IPR plot indicates a greater degree of density localization, with a value of one meaning that the entire Kohn-Sham orbital is contributed by the basis set of a single atom. Such an analysis allows quantitative identification

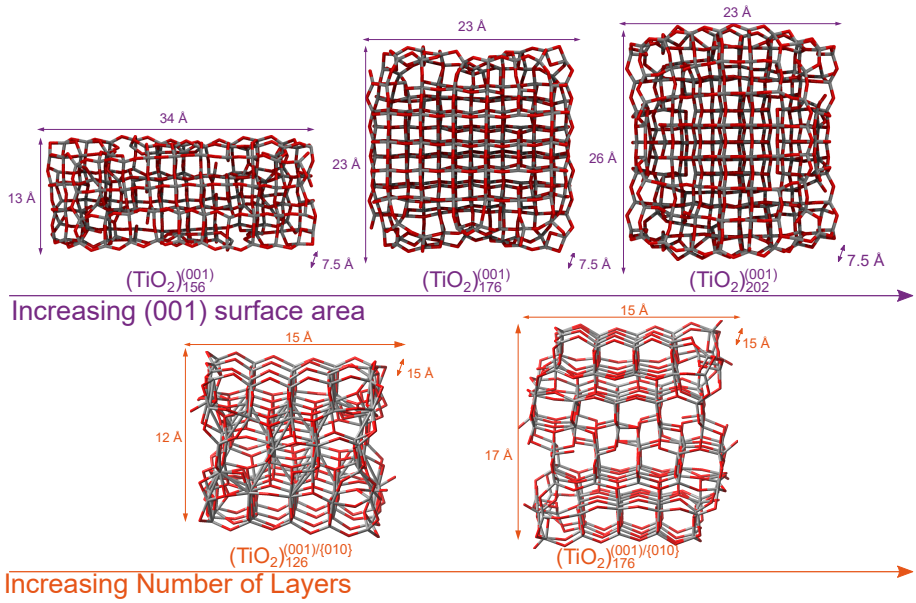

FIGURE 9 Larger $(TiO_2)_n^{(001)}$ and $(TiO_2)_n^{(001)/\{010\}}$ optimized particles. The former are characterized by an increase in the exposed (001) surface area, while the latter are characterized by increased bulk regions.

of the nature of frontier orbital and intra-bandgap defect states.

The results from the IPR analysis (Fig. S9) reflect the erratic nature of the orbital energy trends (Fig. 5). The large decrease in the ionization potential for the directly optimized particles is caused by a number of highly localized defect states in the band gap. States of this nature comprise HOMO and LUMO for the large 82- and 112-unit particles, indicating that removal of such states cannot be accomplished simply by increasing particle size. These states lead to significant disruption of the defined valence and conduction bands, clearly evidenced in the density of states profile (DoS) (Fig. 6). In general, both $(NVE)_c$ and $(NVE)_f$ preparations help in some degree to remove these intra-bandgap defect states. However, particles with the $(NVE)_c$ preparation still show some propensity for formation of localized states on the edge of the valence band, particularly notable in the $(TiO_2)_{82}^{(001)}$ and $(TiO_2)_{112}^{(001)}$ particles. The more disordered structures created by annealing and $(NVE)_f$ preparation result in more delocalized bulk-like electronic structures.

Frontier molecular orbitals (all particles and optimization methods are available in SI, Figs. S16-39) confirm the IPR analysis of the nature of intra-band and band edge states. Interestingly, when the direct optimization procedure predicts a significantly delocalized electronic structure, the $(NVE)_{c/f}$ preparations do little to change the locations of the frontier orbitals. Rather, the location of frontier orbitals appear to depend largely on facet intersections cut into the original structure. However, in the cases where direct optimization predicts numerous intra-band gap defect states, $(NVE)_{c/f}$ can drastically change the nature of the frontier orbitals. For example, the density in the directly optimized $(TiO_2)_{82}^{\{101\}}$ (Fig. 7a) is largely focused on the edges of the nanoparticle at the {101}|{101} facet intersection. These intra-band gap defect states are largely composed of highly localized Ti *d* orbitals on the nanoparticle surface. The $(NVE)_f$ $(TiO_2)_{82}^{\{101\}}$ (Fig. 7b) conversely shows much more delocalization of the frontier orbitals, with large regions of density of the edges of the nanoparticle. Thus, the extensive reconstruction induced by $(NVE)_f$ preparation is successful at removing many of these defect states allowing some of the density to shift to the core of the nanoparticle. A

similar effect is observed in the directly optimized and $(NVE)_f$ $(TiO_2)_{82}^{(001)}$ particle (Fig. 8a and b). However, it is critical to note the amount of reconstruction required to achieve a substantially delocalized electronic structure in this particle. In such cases, the geometric changes likely render the surfaces unrepresentative of the target facet. Therefore, the next section discusses alternative nanoparticle morphologies with large regions of (001) facet in order to study particles that possess a substantially delocalized electronic structure without high degrees of surface reorganization.

3.2 | Mitigating reconstruction for (001) particles

There are two ways to alter the amount of reconstruction of the (001) surface by modification of the morphology of the particle (Fig. 9). The first involves increasing the number of "subsurface" layers in the z-dimension. This is similar to the approach used in planewave calculations of TiO_2 surfaces where one of the relevant structural parameters is the thickness of the slab. In doing so, additional facets are introduced to the nanoparticle, but the area spanned by the (001) surface is unchanged. We created two of these particles with 126- and 176-TiO_2 units and dimensions of 15 x 15 x 12 Å and 15 x 15 x 17 Å with 6 and 8 layers, respectively. These particles are named $(TiO_2)_n^{(001)/\{010\}}$ to emphasize the creation of an additional facet. An alternative approach is to maintain the slab thickness in the z-direction, and increase the area of the (001) surface in x- and y-dimensions, as was done with the $(TiO_2)_{60}^{(001)}$, $(TiO_2)_{82}^{(001)}$, and $(TiO_2)_{112}^{(001)}$ particles. Additional particles with sizes 13 x 34 x 8 Å, 23 x 23 x 8 Å, 26 x 23 x 8 Å and 156-, 176-, and 202-TiO_2 units, respectively, were created. Both methods result in a significant increase in the number of atoms. Comparing both methods will allow the most efficient way to model (001) majority particles with least computational expense to be determined. All particles were prepared with the $(NVE)_f$ protocol, with the exception of $(TiO_2)_{176}^{(001)}$ which possess corner vacancies as opposed to face vacancies. Due to the large sizes of the nanoparticles considered in this section and thus large separation of V_{Ti}, the corner vacancies have a reduced effect on the properties.

To quantify the amount of geometric reconstruction of the (001) facet, the Ti–O–Ti bond angles were measured, as these are the primary reconstruction seen on the (001) surface, as opposed to distortion of individual Ti–O octahedra, which would be detectable in the Ti–O bond lengths or O–Ti–O bond angles. The ideal (001) anatase surface would possess a single O–Ti–O bond angle peak at approximately 156°. For the $(TiO_2)_n^{(001)}$ particles, this bond angle distribution is fairly constant (purple lines in Fig. 10a) as particle size increases. However, none of the particles capture a single peak. For the $(TiO_2)_n^{(001)/\{010\}}$ (orange lines in Fig. 9a) particles, the 176-unit particle shows two very sharp peaks at approximately 125° and 140°. The significant decrease in the Ti–O–Ti angle in all samples compared to the ideal crystal value is due to arching of the bridging O upwards on the surfaces. The sharpness of the peaks in the $(TiO_2)_n^{(001)/\{010\}}$ particles compared to the $(TiO_2)_n^{(001)}$ particles that indicates that increasing the number of subsurface layers is a more efficient way of reducing (001) surface reconstruction and preparing particles with large regions of this facet.

The LUMO-HOMO gap for the two $(TiO_2)_n^{(001)/\{010\}}$ particles is fairly consistent at 4.4 eV (Fig. 10b). There is a reduction in the LUMO-HOMO gap for the $(TiO_2)_n^{(001)}$ particles that gradually converged to the $(TiO_2)_n^{(001)/\{010\}}$ value, calculated at 3.4 eV, 4.2 eV and 4.3 eV for $(TiO_2)_{156}^{(001)}$, $(TiO_2)_{176}^{(001)}$, $(TiO_2)_{202}^{(001)}$, respectively. The DoS (Fig. 10c) shows that this reduction of band gap is related to bleeding of the valence band edge in the$(TiO_2)_{156}^{(001)}$ and $(TiO_2)_{176}^{(001)}$, which eventually disappears as the band gap approaches its limit. There is also significant red-shifting of the valence band edge in the $(TiO_2)_n^{(001)}$ particles. The IPR analysis does not predict significant differences in the nature of the orbitals comprising the band edges (Fig. S10). However, for $(TiO_2)_{126}^{(001)/\{010\}}$, HOMO is located on the {010} surface O *2p* orbitals, while LUMO is delocalized in the subsurface layer below the (001) facet (Fig. S11). Conversely, the HOMO for the $(TiO_2)_{176}^{(001)/\{010\}}$ particle is located in the nanoparticle core and the LUMO is a defect state that occurs on the (001)/{010} intersection (Fig. S12). Conversely for the slabs, HOMOs localize along the edges

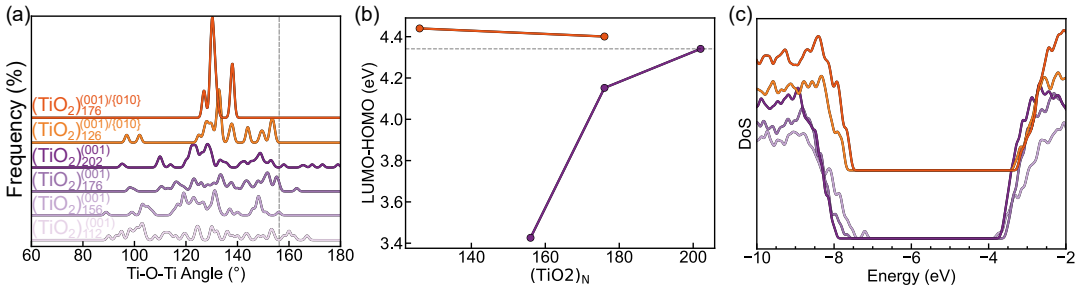

FIGURE 10 Ti–O–Ti bond angles of the (001) surface (a), LUMO-HOMO gap (b) and DoS (c) for larger $(TiO_2)_n^{(001)}$ and $(TiO_2)_n^{(001)/\{010\}}$ particles.

or corners on the surface layer for each of the particles studied here, while LUMOs localize in a similar area, but in the subsurface layer of the nanocrystal (Figs. S13-15). Thus, generating particles with core bulk-like regions as opposed to large surface areas is more efficient for generating a more delocalized electronic structure.

4 | CONCLUSION

Overall, this research demonstrates the care that must be taken when designing oxide nanoparticle models. By performing full quantum chemical optimization and characterization on a range of structurally inter-related nanoparticles, this research provides rationale behind selecting various design choices, including particle shape, size, defects, and optimization procedure, for particle models. These design principles are only generalizable due to the removal of confounding variables like chemical formula and shape. This is the first direct study of size and shape on TiO_2 nanoparticle properties. Taken altogether, the results of the energetic, geometric, and electronic analysis indicate that the $(NVE)_f$ preparations balance maintaining the geometric characteristics of experimental faceted particles, while removing high energy surface reconstructions that result in difficult optimization, and thus providing a reasonable electronic structure and more thermodynamically favorable particle.

Specifically, for the $(TiO_2)_n^{\{101\}}$ particles, direct optimization with DFT leads to highly strained surfaces that are responsible for the large number of defect states found in the DoS and IPR analysis, making them unrepresentative of experimentally sized systems. Pre-optimization that allows traversal of more of the potential energy surface than DFT optimization alone is needed to push a cut structure away from a strained local minima to a more useful structure. Interestingly, the $(NVE)_f$ preparation produces more bulk-like and energetically favorable particles than $(NVE)_c$ in the $(TiO_2)_n^{\{101\}}$ particles without approaching amorphous behavior, in contrast to current practice in model design to remove the least coordinated Ti atoms first. However, for $(NVE)_f$ particles properties like the LUMO-HOMO gap begin to show convergence for differently shaped nanoparticles, indicating that this preparation removes property-defining structural features. There appears to be little effect on the size and surface-bulk ratio when comparing among $(TiO_2)_{60}^{\{101\}}$,$(TiO_2)_{82}^{\{101\}}$,$(TiO_2)_{112}^{\{101\}}$, which suggests that larger {101}-majority nanoparticles may not be necessary to produce results that can be safely extrapolated to experimentally-sized particles.

The same modeling criteria is not entirely extendable to the $(TiO_2)_n^{(001)}$ set of particles. Indeed, direct optimizations of such particles are more highly prone to unphysical disruption of the electronic properties, as clearly demonstrated with the $(TiO_2)_{82}^{(001)}$ particle. The $(NVE)_c$ optimization is moderately successful at mitigating such bleeding of defined band edges, however they continue to be a misrepresentation of expected orbitals for larger nanoparticles

with large (001) regions. The more aggressive $(NVE)_f$ procedure that was most successful in mitigating the formation of these states in the $(TiO_2)_n^{\{101\}}$ particles is also problematic as it leads to so much reconstruction in these particles that they are longer geometrically representative the targeted surface. This also renders the particles unsuitable to model experimentally-sized nanoparticles. We showed that the most efficient way to mitigate these types of reconstruction is by generating particles with core bulk-like regions, opposed to increase the surface area of the particle. Specifically, a 202-unit (001) majority particle was required to approach by the $(TiO_2)_{126}^{(001)/\{010\}}$ particle.

Acknowledgements

We acknowledge financial support from Lehigh University and research computing resources provided by Lehigh University and the TG-CHE190011 allocation from Extreme Science and Engineering Discovery Environment (XSEDE), which is supported by National Science Foundation grant number ACI-1548562 and the NSF CC* Compute program through grant OAC-2019035.

Supporting Information

Supporting Info here

references

1. Randy Pat Sabatini, William T. Eckenhoff, Alexandra Orchard, Kacie R. Liwosz, Michael R. Detty, David F. Watson, David W. McCamant, Richard Eisenberg, *J. Am. Chem. Soc.* **2014**, *136* (21).
2. Elena Jakubikova, David N. Bowman, *Acc. Chem. Res.* **2015**, *48* (5).
3. Qing Kang, Junyu Cao, Yuanjian Zhang, Lequan Liu, Hua Xu, Jinhua Ye, *J. Mater. Chem.A* **2013**, *1* (18).
4. Mohammed Ismael, *Sol. Energy* **2020**, *211*.
5. Lorenzo Mino, Giuseppe Spoto, Anna Maria Ferrari, *J. Phys. Chem. C* **2014**, *118* (43).
6. Severin N. Habisreutinger, Lukas Schmidt-Mende, Jacek K. Stolarczyk, *Angew. Chem. Int. Ed.* **2013**, *52* (29).
7. Ping-Quan Wang, Yang Bai, Jian-Yi Liu, Zhou Fan, Ya-Qin Hu, *Catal. Commun.* **2012**, *29*.
8. Hua Gui Yang, Cheng Hua Sun, Shi Zhang Qiao, Jin Zou, Gang Liu, Sean Campbell Smith, Hui Ming Cheng, Gao Qing Lu, *Nature* **2008**, *453* (7195).
9. Hengzhong Zhang, Jillian F. Banfield, *Chem. Rev.* **2014**, *114* (19).
10. Anusorn Kongkanand, Kevin Tvrdy, Kensuke Takechi, Masaru Kuno, Prashant V. Kamat, *J. Am. Chem. Soc.* **2008**, *130* (12).
11. Yahya Alivov, Z. Y. Fan, *J. Phys. Chem. C* **2009**, *113* (30).
12. Thomas R. Gordon, Matteo Cargnello, Taejong Paik, Filippo Mangolini, Ralph T. Weber, Paolo Fornasiero, Christopher B. Murray, *J. Am. Chem. Soc.* **2012**, *134* (15).
13. Tim Würger, Wolfgang Heckel, Kai Sellschopp, Stefan Müller, Andreas Stierle, Yuemin Wang, Heshmat Noei, Gregor Feldbauer, *J. Phys. Chem. C* **2018**, *122* (34).
14. Kenji Shirai, Gianluca Fazio, Toshiki Sugimoto, Daniele Selli, Lorenzo Ferraro, Kazuya Watanabe, Mitsutaka Haruta, Bunsho Ohtani, Hiroki Kurata, Cristiana Di Valentin, Yoshiyasu Matsumoto, *J. Am. Chem. Soc.* **2018**, *140* (4).

15. Federico A. Soria, Cristiana Di Valentin, *Nanoscale* **2021**, *13* (7).

16. Kyoung Chul Ko, Stefan T. Bromley, Jin Yong Lee, Francesc Illas, *The Journal of Physical Chemistry Letters* **2017**, *8* (22).

17. Angel Morales-García, Antoni Macià Escatllar, Francesc Illas, Stefan T. Bromley, *Nanoscale* **2019**, *11* (18).

18. Oriol Lamiel-Garcia, Kyoung Chul Ko, Jin Yong Lee, Stefan T. Bromley, Francesc Illas, *J. Chem. Theory Comput.* **2017**, *13* (4).

19. A. S. Barnard, L. A. Curtiss, *Nano Lett.* **2005**, *5* (7).

20. Daniel R. Hummer, James D. Kubicki, Paul R. C. Kent, Jeffrey E. Post, Peter J. Heaney, *J. Phys. Chem. C* **2009**, *113* (11).

21. Francesca Nunzi, Loriano Storchi, Michele Manca, Roberto Giannuzzi, Giuseppe Gigli, Filippo De Angelis, *ACS Applied Materials & Interfaces* **2014**, *6* (4).

22. Vladimir S. Naumov, Anastasiia S. Loginova, Alexander A. Avdoshin, Stanislav K. Ignatov, Alexey V. Mayorov, Bálint Aradi, Thomas Frauenheim, *Int. J. Quantum Chem.* **2021**, *121* (2).

23. Jun-ichi Fujisawa, Shunsuke Kato, Minoru Hanaya, *Chem. Phys. Lett.* **2022**, *788*.

24. Maria J. Lundqvist, Mattias Nilsing, Petter Persson, Sten Lunell, *Int. J. Quantum Chem.* **2006**, *106* (15).

25. Hong Wang, James P. Lewis, *physica status solidi (b)* **2011**, *248* (9).

26. Marta Gałyńska, Petter Persson, *Int. J. Quantum Chem.* **2013**, *113* (24).

27. Filippo De Angelis, Cristiana Di Valentin, Simona Fantacci, Andrea Vittadini, Annabella Selloni, *Chem. Rev.* **2014**, *114* (19).

28. Gianluca Fazio, Lara Ferrighi, Cristiana Di Valentin, *J. Phys. Chem. C* **2015**, *119* (35).

29. Petter Persson, J. Christof M. Gebhardt, Sten Lunell, *J. Phys. Chem. B* **2003**, *107* (15).

30. Yarkın Aybars Çetin, Benjamí Martorell, Francesc Serratosa, Neus Aguilera-Porta, Monica Calatayud, *J. Phys.: Condens. Matter* **2022**, *34* (31).

31. Ángel Morales-García, Oriol Lamiel-García, Rosendo Valero, Francesc Illas, *J. Phys. Chem. C* **2018**, *122* (4).

32. J. He, R.K. Behera, M.W. Finnis, X. Li, E.C. Dickey, S.R. Phillpot, S.B. Sinnott, *Acta Mater.* **2007**, *55* (13).

33. A S Barnard, *Rep. Prog. Phys.* **2010**, *73* (8).

34. Daniele Selli, Gianluca Fazio, Cristiana Di Valentin, *The Journal of Chemical Physics* **2017**, *147* (16).

35. Antoni Macià Escatllar, Angel Morales-García, Francesc Illas, Stefan T. Bromley, *The Journal of Chemical Physics* **2019**, *150* (21).

36. Craig Vandervelden, Amy Jystad, Baron Peters, Marco Caricato, *Industrial & Engineering Chemistry Research* **2021**, *60* (35).

37. J. C. Boettger, *Phys. Rev. B* **1994**, *49* (23).

38. Vincenzo Fiorentini, M Methfessel, *J. Phys.: Condens. Matter* **1996**, *8* (36).

39. M. J. Frisch, G. W. Trucks, H. B. Schlegel, G. E. Scuseria, M. A. Robb, J. R. Cheeseman, G. Scalmani, V. Barone, G. A. Petersson, H. Nakatsuji, X. Li, M. Caricato, A. V. Marenich, J. Bloino, B. G. Janesko, R. Gomperts, B. Mennucci, H. P. Hratchian, J. V. Ortiz, A. F. Izmaylov, J. L. Sonnenberg, D. Williams-Young, F. Ding, F. Lipparini, F. Egidi, J. Goings, B. Peng, A. Petrone, T. Henderson, D. Ranasinghe, V. G. Zakrzewski, J. Gao, N. Rega, G. Zheng, W. Liang, M. Hada, M. Ehara, K. Toyota, R. Fukuda, J. Hasegawa, M. Ishida, T. Nakajima, Y. Honda, O. Kitao, H. Nakai, T. Vreven, K. Throssell, J. A. Montgomery, Jr., J. E. Peralta, F. Ogliaro, M. J. Bearpark, J. J. Heyd, E. N. Brothers, K. N. Kudin, V. N. Staroverov, T. A. Keith, R. Kobayashi, J. Normand, K. Raghavachari, A. P. Rendell, J. C. Burant, S. S. Iyengar, J. Tomasi, M. Cossi, J. M. Millam, M. Klene, C. Adamo, R. Cammi, J. W. Ochterski, R. L. Martin, K. Morokuma, O. Farkas, J. B. Foresman, D. J. Fox, *Gaussian~16 Revision C.01*, **2016**, Gaussian Inc. Wallingford CT.

40. Axel D. Becke, *The Journal of Chemical Physics* **1993**, *98* (7).

41. Y. Bouteiller, C. Mijoule, M. Nizam, J.C. Barthelat, J.P. Daudey, M. Pelissier, B. Silvi, *Mol. Phys.* **1988**, *65* (2).

42. Aidan P. Thompson, H. Metin Aktulga, Richard Berger, Dan S. Bolintineanu, W. Michael Brown, Paul S. Crozier, Pieter J. in 't Veld, Axel Kohlmeyer, Stan G. Moore, Trung Dac Nguyen, Ray Shan, Mark J. Stevens, Julien Tranchida, Christian Trott, Steven J. Plimpton, *Comput. Phys. Commun.* **2022**, *271*.

43. Masanori Matsui, Masaki Akaogi, *Mol. Simul.* **1991**, *6* (4-6).

44. Roy Dennington, Todd A. Keith, John M. Millam, *GaussView Version 6*, **2019**, Semichem Inc. Shawnee Mission KS.

45. Kulbir Kaur Ghuman, Chandra Veer Singh, *J. Phys.: Condens. Matter* **2013**, *25* (47).

46. David Mora-Fonz, Moloud Kaviani, Alexander L. Shluger, *Phys. Rev. B* **2020**, *102* (5).

47. Hengzhong Zhang, Bin Chen, Jillian F. Banfield, Glenn A. Waychunas, *Phys. Rev. B* **2008**, *78* (21).

48. Hakon Wadell, *The Journal of Geology* **1935**, *43* (3).

49. I. Gonzalo-Juan, A. J. Krejci, M. A. Rodriguez, Y. Zhou, K. A. Fichthorn, J. H. Dickerson, *Appl. Phys. Lett.* **2014**, *105* (11).

50. Wen Yan, Shuiqing Li, Yiyang Zhang, Qiang Yao, Stephen D. Tse, *J. Phys. Chem. C* **2010**, *114* (24).

51. André A. Lino, Hélio Chacham, Mário S. C. Mazzoni, *J. Phys. Chem. C* **2011**, *115* (37).